

# Key residue for aggregation of amyloid- $\beta$ peptides

**Satoru Itoh**

Institute for Molecular Science <https://orcid.org/0000-0002-2638-663X>

**Maho Yagi-Utsumi**

National Institutes of Natural Sciences <https://orcid.org/0000-0001-8144-740X>

**Koichi Kato**

National Institutes of Natural Sciences <https://orcid.org/0000-0001-7187-9612>

**Hisashi Okumura** (✉ [hokumura@ims.ac.jp](mailto:hokumura@ims.ac.jp))

National Institutes of Natural Sciences

---

## Article

**Keywords:**

**Posted Date:** February 24th, 2022

**DOI:** <https://doi.org/10.21203/rs.3.rs-1337043/v1>

**License:**  This work is licensed under a Creative Commons Attribution 4.0 International License.

[Read Full License](#)

---

# Abstract

Amyloid- $\beta$  peptides (Abs) are associated with Alzheimer's disease and have two isoforms: Ab40 and Ab42. Although the difference between Ab40 and Ab42 is only two additional C-terminal residues, Ab42 aggregates much faster and is more toxic than Ab40. It is unknown what role the C-terminal two residues play in accelerating aggregation. Clarifying the differences between the oligomerization processes of Ab40 and Ab42 is essential to elucidate the key factors of oligomerization. Performing Hamiltonian replica-permutation molecular dynamics simulations for Ab40 and Ab42 to investigate the early oligomerization process, we identified the key residue, Arg5, for the Ab42 dimerization. The two additional residues in Ab42 allow the C-terminus to form contact with Arg5, and this contact stabilizes the  $\beta$ -hairpin. This  $\beta$ -hairpin promotes the intermolecular  $\beta$ -bridge formation. We also conducted experiments on Ab aggregations to validate these simulation results and confirmed that mutations of Arg5 remarkably suppressed the Ab42 aggregation.

## Introduction

It is known that more than 40 proteins and peptides form aggregates associated with human diseases, such as Alzheimer's disease (AD), Parkinson's disease, and hemodialysis-related amyloidosis<sup>1-4</sup>. An example of such a peptide is the amyloid- $\beta$  peptide (Ab). Abs form soluble oligomers and insoluble amyloid fibrils by their aggregation. These aggregates play a vital role in the pathogenesis of AD<sup>5,6</sup>. Amyloid fibrils of Ab are known to form cross- $\beta$ -sheet structures<sup>7,8</sup>. Additionally, their atomic-level structures have been reported by experiments using solid-state nuclear magnetic resonance (NMR) spectroscopy<sup>9-12</sup> and cryogenic electron microscopy (cryo-EM)<sup>13,14</sup>. Although it has been shown by NMR experiments that oligomers also form  $\beta$ -sheet structures<sup>15,16</sup>, their atomic-level structures have yet to be clarified.

Ab is produced by the proteolytic processing of amyloid precursor protein<sup>17</sup>. Although there are several Abs with different numbers of amino-acid residues, the main isoforms have 40 (Ab40) and 42 (Ab42) amino-acid residues<sup>18,19</sup>. The only difference between Ab40 and Ab42 is that Ab42 has two additional residues at its C-terminus. However, Ab42 is more toxic than Ab40<sup>20</sup> and is the major component of early senile plaques in the brains of AD patients<sup>21-23</sup>. It is also known that in several early-onset familial ADs, the production of Ab42 increases<sup>24-27</sup>. Additionally, Ab42 forms oligomers and amyloid fibrils more rapidly than Ab40<sup>28,29</sup>. The two C-terminal residues of Ab42 play essential roles in the rapid aggregation, but the details have not been elucidated. Elucidating the difference between the oligomerization processes of Ab40 and Ab42 is essential to understand Ab aggregation and overcome AD.

To investigate Ab at the atomic level, all-atom molecular dynamics (MD) simulation is essential. Many studies have used MD simulation on aggregation and disaggregation of Ab<sup>30-51</sup>. For studies on the oligomerization process, most studies have employed Ab fragments, such as Ab(16-22)<sup>52-58</sup>, Ab(10-35)<sup>59</sup>, and Ab(29-42)<sup>60-63</sup>. Several studies have been reported for oligomer formation of full-length

Abs<sup>64–66</sup>. It has been shown that A $\beta$ 40 dimers form various secondary structures, such as intramolecular and intermolecular  $\beta$ -sheet structures and  $\alpha$ -helix structures<sup>64</sup>. Similar results were reported for A $\beta$ 42 dimers<sup>65</sup>. Because Ab oligomerization is a slow process for all-atom MD simulation, most of these studies used the replica-exchange method (REM)<sup>67, 68</sup> to obtain efficient samplings of Ab structures<sup>66</sup>.

Recently, replica-permutation method (RPM) has been proposed<sup>69</sup> to enhance sampling efficiency more than REM. In this method, similar to REM, copies (replicas) of a target system are prepared. These replicas are assigned different temperatures to perform canonical simulations. During simulations, the assigned temperatures are permuted among more than two replicas, whereas they are exchanged between two replicas in REM. Additionally, instead of the Metropolis algorithm<sup>70</sup>, the Suwa–Todo algorithm<sup>71</sup> is used to minimize the rejection ratio for replica-permutation trials. Then, the Hamiltonian RPM (HRPM) was proposed to generalize RPM<sup>72</sup>. In HRPM, the same temperature is assigned to all replicas. However, different values of a parameter introduced in the Hamiltonian are assigned and permuted among more than two replicas. The dimer and larger oligomer formation processes of Ab fragments have been elucidated using this HRPM<sup>62, 63</sup>.

It is necessary to clarify the difference in oligomerization between Ab40 and Ab42 at the atomic level to elucidate the key factors of the Ab aggregation. However, no study has shown the differences in these oligomerization processes at the atomic level. Therefore, in this paper, we investigated the dimerization process, which is the early oligomerization process, for these Abs using MD simulation. We employed the Coulomb RPM (CRPM)<sup>72</sup> to enhance conformational sampling for Abs in an explicit solvent. CRPM is a form of HRPM. It is a useful method for investigating the aggregation processes of biomolecules. As a result of the CRPM simulation, we identified a key residue in dimerization. We also conducted experiments on Ab aggregation to verify whether the residue identified by our simulation is actually important for the aggregation process. Consequently, we obtained that Ab aggregation is significantly suppressed by mutating the residue identified in the simulation.

## Methods

**CRPMD Simulations of Two Ab Molecules.** To investigate the dimerization process of Ab40 and Ab42, we applied the Coulomb replica-permutation MD (CRPMD) method to two Ab40 molecules and two Ab42 molecules. The N-termini and C-termini were left uncapped. The two Ab molecules were put in a cubic unit cell with explicit water molecules and counter ions. The side lengths of the cubic unit cells were 101.7 Å in both Ab systems (i. e., a system containing two Ab40 molecules and that containing two Ab42 molecules). Periodic boundary conditions were utilized. The Amber parm99SB force field<sup>73</sup> and TIP3P rigid-body model<sup>74</sup> were employed for the Ab and water molecules, respectively. The SHAKE algorithm was used to constrain bond lengths with the hydrogen atoms of Ab and fix the water molecule structures during the simulations. The cutoff distance for the Lennard-Jones potential energy was 12.0 Å. The electrostatic potential energy was calculated using the particle mesh Ewald method<sup>75</sup>. The temperature was controlled by the Nosé–Hoover thermostat<sup>76–79</sup>. The multiple time-step method<sup>80</sup> was employed,

and the time steps were taken to be 4.0 fs for interactions between the water molecules and 1.0 fs for other interactions. Initial conformations for these CRPMD simulations were the same for all replicas; they were prepared as presented in the Supplementary Information. The number of replicas was 18. The values of the parameter  $\lambda$  for the CRPM were set as 0.82, 0.84, 0.86, 0.88, 0.90, 0.92, 0.94, 0.96, 0.98, 1.00, 1.01, 1.02, 1.03, 1.04, 1.05, 1.06, 1.07, and 1.08. CRPM is also described in the Supplementary Information. The 18 replicas were divided into three subsets, and each subset had six replicas and six parameter values (see Ref. <sup>69</sup> for more details). Each CRPMD simulation was performed for 1.12 ms at 350 K per replica, including an equilibration run performed for 100.0 ns. The production run of each Ab system was conducted for 18.36 ms in total. The trajectory data were stored every 2.0 ps, and trials of replica permutations were performed every 4.0 ps.

We employed the reweighting techniques<sup>81,82</sup> to obtain the physical quantities at the original parameter ( $\lambda = 1.00$ ) in the Results and Discussion section. The errors were estimated using the jackknife method<sup>83</sup>. The number of bins for the jackknife method was 20.

**MD Simulations of the Ab42 Monomer.** We also performed MD simulations of the Ab42 monomer to investigate the effect of Arg5 on the stability of the b-hairpin. We employed two different b-hairpins as the initial structures, as shown in Fig. S2. The Ab42 molecule was put in a cubic unit cell. The side length of the cubic unit cell was 64.2 Å. Ten different initial velocities were employed for each initial structure, meaning that we employed 20 different initial conditions. For each initial condition, an MD simulation was performed for 320.0 ns. The other simulation conditions were the same as in the previous subsection. For comparison, we performed MD simulations of two Ab42 mutants: R5G and R5E. Two initial structures were also employed for each mutant, and their structures were the same as those for the wild type, except for the sidechain of residue 5. For each initial structure, ten different initial velocities were also employed. The other simulation conditions were the same as for the wild type.

**Experiments.** The synthetic wild-type Ab42 and Ab40 peptides were purchased from Toray Research Center, Inc. The synthetic Ab42 and Ab40 peptides with a substitution of Arg5 to Gly (R5G) or Glu (R5E) were purchased from Abclonal. The peptides were dissolved in 6 M guanidine hydrochloride and purified using a Superdex 75 Increase 10/300 column (Cytiva) at a 0.4 ml/min flow rate with 20 mM sodium phosphate buffer, a pH of 7.4, to remove from potential aggregated species. The obtained monomer was diluted with 20 mM sodium phosphate buffer, a pH of 7.4, to the desired concentration and supplemented with 0.1 mM Thioflavin T (ThT) from a 2 mM stock solution. Then, each sample was pipetted into multiple wells of a 96-well half-area, low-binding polyethylene glycol coating plate with a clear bottom (Corning 3881) at 0.1 mL per well. Aggregation assays were initiated by placing the 96-well plate at 37°C under quiescent conditions in a plate reader (Infinite 200Pro, TECAN). The ThT fluorescence was measured through the bottom of the plate with a 430-nm excitation filter and a 485-nm emission filter. The ThT fluorescence was followed for three repeats of each sample.

## Results And Discussion

**Comparison of Ab42 and Ab40 dimerization.** To investigate whether there is a difference in dimer formation, which is the smallest unit of oligomer formation, we first calculated probabilities of dimer formation for Ab42 and Ab40. Figure 1 shows distributions of oligomer sizes. Here, when two Abs formed more than one intermolecular b-bridge, it was regarded as these Abs formed a dimer. The DSSP (define secondary structure of proteins) criteria<sup>84</sup> were used to determine secondary structures. As shown in the figure, Ab42 has a slightly higher probability of dimer formation than Ab40. Conversely, Ab40 tends to be in a monomer state compared to Ab42. This tendency and probabilities of the monomer states are consistent with experimental results that showed oligomer size distributions for Ab42 and Ab40<sup>85</sup>.

Next, we calculated the intermolecular contact probabilities of C<sub>α</sub> atoms to see the dimer structure. Figures 2a and 2b show the intermolecular contact probability for Ab42 and Ab40, respectively. Here, when the distance between a pair of C<sub>α</sub> atoms was less than 6.5 Å, it was regarded as a contact. In the Ab42 dimer, the b1 and b2 regions tended to form an intermolecular antiparallel b-sheet, as shown by the magenta ellipse in Fig. 2a. Here, the b1 and b2 regions consist of residues 17–21 and C-terminal residues after residue 29, respectively. These hydrophobic regions have been reported to form b-sheets in amyloid fibrils<sup>9–14</sup>. An intermolecular parallel b-sheet was also formed moderately between the b1 regions (the black ellipse). In the Ab40 dimer, an intermolecular antiparallel b-sheet was mainly formed between the b1 and b2 regions, as shown in Fig. 2b (the magenta ellipse).

To investigate the lengths of b-strands composing the intermolecular b-sheet and identify residues in the b-strands, we calculated the probabilities of intermolecular b-bridge formation of residues at each length of the b-strand. Here, the b-strand length is the number of consecutive residues that form the b-strand, and the formation of longer b-strands stabilizes the intermolecular b-sheet. Figures 2c and 2d show the probabilities for Ab42 and Ab40, respectively. As shown by the magenta ellipse in Fig. 2c, the b-strand length with the highest probability was three. As shown in Figs. 2a and 2c, in the Ab42 dimer, the intermolecular antiparallel b-sheet between the b1 and b2 regions was composed of the b-strands consisting of three residues. In contrast, in the Ab40 dimer, the intermolecular antiparallel b-sheet had only one b-bridge (i.e., length of the b-strand is one), as shown in Figs. 2b and 2d. This means that the Ab42 dimer had a more stable intermolecular b-sheet than the Ab40 dimer.

There were differences not only in the intermolecular structures but also in the intramolecular structures between Ab42 and Ab40. Figure 3 shows the intramolecular contact probabilities of C<sub>α</sub> atoms. Ab42 formed a b-hairpin between the b1 and b2 regions, as shown by the magenta ellipse in Fig. 3a. However, in Ab40, such b-hairpin was rarely formed (Fig. 3b). This difference in b-hairpin formation affects the difference in intermolecular b-sheet formation between Ab42 and Ab40. This is because two of the authors (S. G. I. and H. O.) reported that a b-hairpin of an Ab fragment readily formed intermolecular b-sheets with other Ab fragments<sup>62</sup>. In our simulation of full-length Abs, we also observed that the b-hairpin formed intermolecular b-sheets with the other Ab, as seen in the movies. In these movies, two Ab42 that are spatially separated approach each other (Movie S1), and one Ab42 forms the b-hairpin (Movie S2) and then forms the intermolecular b-sheet with the other Ab (Movie S3). It is worth noting that the value

of  $\beta$  varies throughout the movies since these movies are the trajectory in one replica in the CRPMD simulation. Additionally, not only our works but also several experimental and computational works have shown that the  $\beta$ -hairpins accelerate intermolecular  $\beta$ -sheet formation<sup>86–88</sup>.

To investigate the relationship between intramolecular and intermolecular  $\beta$ -bridges, we calculated the probability distributions with respect to the number of intramolecular and intermolecular  $\beta$ -bridges. Figure 4 shows the probability distributions for Ab42 and Ab40. In both systems, the probability of forming more intermolecular  $\beta$ -bridges is higher when more intramolecular  $\beta$ -bridges are formed, as shown by magenta circles. This indicates that an intermolecular  $\beta$ -sheet is readily formed in the presence of a  $\beta$ -hairpin. In other words, the  $\beta$ -hairpin stabilizes the intermolecular  $\beta$ -sheet. Therefore, the reason why Ab42 forms a more stable intermolecular  $\beta$ -sheet is that Ab42 tends to form the  $\beta$ -hairpin in comparison with Ab40.

The mechanism by which the  $\beta$ -hairpin promotes the formation of the intermolecular  $\beta$ -sheet structure is as follows. The formation of the  $\beta$ -hairpin maintains the extended structures in the b1 and b2 regions and leaves their hydrophobic sidechains exposed in the aqueous solution. These exposed hydrophobic sidechains attract the hydrophobic sidechains in the b1 and b2 regions of the other Ab. Since the two Abs are close and Ab that forms the hairpin has the extended structures in the b1 and b2 regions, an intermolecular  $\beta$ -sheet is quickly formed when Ab that does not form the hairpin forms an extended structure in the b1 or b2 regions.

Such a mechanism of  $\beta$ -sheet formation has been reported for other molecules, such as a designed peptide that forms  $\alpha$ -helix and  $\beta$ -hairpin in equal proportions<sup>89–92</sup>. This peptide was designed by adding seven residues to a fully helical peptide<sup>89</sup>. The region consisting of the additional seven residues was hydrophobic and formed an extended structure. As the extended region approaches the helix region, the hairpin is formed when the helix region forms the extended structure<sup>90–92</sup>. Consequently, this designed peptide can have both  $\alpha$ -helix and  $\beta$ -hairpin.

**Tertiary structures of Ab42 and Ab40 dimers.** Principal component analysis (PCA)<sup>93</sup> was used to observe the tertiary structures of Ab42 and Ab40. Here, to focus on the dimer structure, the conformations (snapshots obtained from our MD simulations) in which two Abs formed more than one intermolecular  $\beta$ -bridge were employed for PCA. Additionally, only the coordinates of C <sub>$\alpha$</sub>  atoms in the b1 and b2 regions were considered to perform PCA. More details of PCA are presented in the Supplementary Information. Figure 5a shows the free-energy landscape for Ab42 with respect to the first and second principal components. Five local-minimum free-energy states (state A–E) are shown in the figure. The representative tertiary structures in these states are also shown in the figure. Each representative structure is as follows (we focus on  $\beta$ -sheet structures of the b1 and b2 regions in two Abs): (state A) The green Ab42 forms a  $\beta$ -hairpin with intramolecular antiparallel  $\beta$ -bridges between the b1 and b2 regions. Intermolecular parallel  $\beta$ -bridges are also formed between the b1 region of this Ab42 and that of the other Ab42. (state B) The blue Ab42 has a  $\beta$ -hairpin structure in which the b1 and b2 regions form intramolecular antiparallel  $\beta$ -bridges. A  $\beta$ -hairpin is also seen in the b2 region in the green Ab42. These two  $\beta$ -hairpins have a  $\beta$ -sheet structure with intermolecular  $\beta$ -bridges between the b1 region in the blue

Ab42 and the b2 region in the green Ab42. (state C) An intermolecular parallel b-bridge is formed between the b1 region in the green Ab42 and the b2 region in the blue Ab42. (state D) The two b2 regions in Ab42s form intermolecular parallel b-bridges. (state E) The green Ab42 has a b-hairpin with b-bridges between the b1 and b2 regions. An intermolecular parallel b-bridges between the two b2 regions are formed. A b-hairpin in the N-terminal region in the blue Ab42 also forms intermolecular parallel b-bridges with the b1 region in the green Ab42.

Figure 5b shows the free-energy landscape for Ab40 with respect to the first and second principal components. There are five local-minimum free-energy states (state A'–E'). The representative tertiary structure in each state is shown in this figure. The representative structures are as follows: (state A') Intermolecular antiparallel b-bridges are formed between the b1 region in the blue Ab42 and the b2 region in the green Ab42. (state B') There are three b-strands in the b1 and b2 regions in the blue Ab42. The b2 region in the green Ab42 forms an intermolecular antiparallel b-sheet with the b1 region in the blue Ab42. (state C') An intermolecular b-bridge is formed between the b2 region in the green Ab42 and the b1 region in the blue Ab42. (state D') The blue Ab42 has a b-hairpin with intramolecular b-bridges between the b1 and b2 regions. The b2 region in the green Ab42 forms intermolecular antiparallel b-bridges with the b1 region in the blue Ab42. (state E') An intermolecular b-bridge is formed between the two b2 regions.

From these representative tertiary structures, in Ab42 and Ab40 dimer, longer b-strand with intermolecular b-bridges tends to be formed when at least one Ab has stable intramolecular b-bridges (*i.e.*, b-hairpin or intramolecular b-sheet). This tendency is consistent with Fig. 4. Thus, the intramolecular b-bridges play an essential role in the formation of the intermolecular b-bridges.

**Key residue for the b-hairpin of Ab42.** To investigate why Ab42 forms more b-hairpin, we calculated the probability of intramolecular contacts, including sidechain atoms. Here, when the shortest distance between atoms included in two different residues was less than 5.0 Å, it was regarded as a contact between the two residues. Hydrogen atoms were not considered in calculating the contact probability. Figure 6 shows the contact probabilities. The contact patterns are almost the same as the intramolecular contacts between C<sub>α</sub> atoms in Fig. 3. However, as shown in Fig. 6a, the contact peaks between the C-terminus and vicinity of residue 5 (Arg5) are more obvious, as indicated by the black circles. This is because these contacts were maintained by the electrostatic interaction between the negative charge of the carboxyl group (COO<sup>-</sup>) in the C-terminus and the positive charge of the guanidinium group in Arg5. Moreover, the positions of the peaks indicated by the black circles are located on the extension of the major axis of the magenta ellipse corresponding to the b-hairpin. Therefore, the contact between the C-terminus and Arg5 contributes to the stabilization of the b-hairpin. Conversely, no peak corresponds to contact between the C-terminus and Arg5 in Ab40 (Fig. 6b).

Figure 7 shows a schematic illustration in which the b-hairpin of Ab42 is stabilized by the contact between the C-terminus and Arg5. Here, a contact between residue 22 (E22) and residue 28 (K28) is also shown. This contact is formed with a high probability due to the electrostatic interaction between their sidechains (*i.e.*, a salt bridge) as in the contact between the C-terminus and Arg5. As long as the contacts

between the C-terminus and Arg5 and between E22 and K28 are maintained, the distance between b1 and b2 regions is inevitably shortened. Additionally, because the number of residues between Arg5 and E22 and between K28 and A42 (C-terminus) are almost equal, both b1 and b2 regions can have extended structures simultaneously. The b-hairpin is formed when the two extended regions are at a short distance. This is the mechanism of stabilizing the b-hairpin of Ab42 by the contact between the C-terminus and Arg5. Regarding Ab40, since the number of residues between K28 and V40 (C-terminus) is less than that between Arg5 and E22, these two regions cannot have extended structures simultaneously. Consequently, Ab40 hardly forms the b-hairpin.

**MD simulations of Ab42 monomer.** To investigate the effects of Arg5 on the stabilization of the b-hairpin, we performed MD simulations of an Ab42 monomer and its mutants. We used R5G and R5E as the mutants. As mentioned in the previous subsection, the electrostatic interaction between Arg5 and C-terminus is expected to be essential to stabilize the b-hairpin. To decrease attractive electrostatic forces between residue 5 and C-terminus, we chose neutral and negative charged residues, Gly and Glu. Figure 8a shows a typical time series of the shortest distance between residue 5 and C-terminal residue atoms for each Ab monomer system. In the wild type, the shortest distance tended to get trapped in the vicinity of 3 Å. This means that the C-terminus is often bound to Arg5. In contrast, such bindings were not seen in the mutants. Figure 8b shows the probability distribution of the shortest distance between residue 5 and C-terminal residue for each system. This distribution was calculated by averaging 20 MD simulations after 100 ns. The distributions show that the binding between Arg5 and C-terminus was frequently formed in the wild type; however, no such binding was formed in the mutants.

To investigate the stability of the b-hairpin, the number of b-bridges between the b1 and b2 regions was counted at each MD step. Figure 8c shows the time series of the average numbers of b-bridges calculated from 20 MD simulations. In the wild type, the number of b-bridges decreased more slowly than in the mutants. This means that the b-bridges between the b1 and b2 regions were maintained in the wild type but were gradually broken in the mutants. Furthermore, the intramolecular contacts between C<sub>α</sub> atoms were calculated to investigate whether the hairpin structures are maintained. Figure 9 shows the contact probabilities obtained from 20 MD simulations after 100 ns. As shown in the figure, the contact patterns corresponding to the hairpin structures in the mutants had lower probabilities than those in the wild type. It means that the hairpin structures of the mutants were gradually broken as the number of b-bridges decreased due to the lack of stable binding between residue 5 and C-terminus. Therefore, the interaction between Arg5 and C-terminus plays an essential role in the formation of the b-hairpin in Ab42.

**Experiments on Ab aggregations.** From our MD simulations, Arg5 is expected to promote the Ab42 aggregation. Conversely, in the mutations of Arg5 to Gly or Glu, their aggregations are expected to be suppressed. To confirm this prediction from our MD simulations, we conducted experiments on the aggregations of the wild type and mutants. Figures 10a, 10b, and 10c show the aggregation of these Ab42s monitored by ThT fluorescence. As expected from the MD simulations, the Ab42 aggregation is suppressed by the mutations of Arg5 to Gly or Glu. The effect of the mutations is remarkable. Thus, in the experiments, it was confirmed that Arg5 plays an essential role in the Ab42 aggregation.

Additionally, we investigated whether Arg5 affects the Ab40 aggregation. Figure 10d, 10e, and 10f show the experimental results on the aggregation of the Ab40 wild type and mutants using ThT assay. Interestingly, mutations of Arg5 also affect the Ab40 aggregation. However, the effect of suppressing aggregation seems to be weaker than that of Ab42. For instance, for R5G of Ab40, although the start of aggregation is delayed, the aggregation is not suppressed much. Therefore, the role of Arg5 in the Ab40 aggregation may be different from that in the Ab42 aggregation. In fact, in our MD simulations for Ab40, the contact between Arg5 and C-terminus seen in Ab42 is hardly formed (Fig. 6b).

To investigate the role of Arg5 in the Ab40 aggregation, we calculated the probability of intermolecular contacts, including sidechain atoms, from our MD simulations. For comparison, we also calculated those for Ab42. Figure 11 shows the contact probabilities for both Abs. In both Abs, as with the intramolecular contacts, the contact patterns are similar to the intermolecular contacts between C<sub>α</sub> atoms in Fig. 2. In Ab42, there is a contact peak between the C-terminus and Arg5 residues, as seen in the intramolecular contacts in Fig. 6a. However, this contact probability is lower than that of the intramolecular contacts in Fig. 6a. This indicates that the intramolecular contact between Arg5 and the C-terminus is more dominant than the intermolecular contact between them. For Ab40, Arg5 has intermolecular contacts with residues in the N-terminal regions, as shown in Fig. 11b (the magenta ellipse). The reason why Arg5 and N-terminal residues form contacts is that there are several negatively charged residues in the N-terminal region, such as Asp1, Glu3, Asp7, and Glu11. In contrast, Arg5 is the only positively charged residue in the N-terminal region, except for the N-terminus (NH<sup>3+</sup>). This contact between Arg5 and N-terminal region plays an essential role in the dimer formation of Ab40. This is because when there is such a contact, the distance between the two Ab40s is shorter; thereby, forming a dimer.

From these simulation results, the experimental results of Ab40 in Fig. 10 can be explained as follows. The total negative charge in the N-terminal region increases by mutating Arg5 to a neutral or negatively charged residue. The larger the total negative charge, the less the N-terminal regions form contacts with each other. Consequently, the Ab40 aggregation is suppressed.

**Known mutations in the vicinity of residue 5.** Several Ab mutants, where the vicinity of residue 5 is mutated, are known in association with AD. For example, rodent Ab has three mutations (R5G, Y10T, and H13R) in the N-terminal region, and it has been shown that age-associated amyloid plaques do not accumulate in rodents<sup>94</sup>. It was reported that this mutant aggregates more slowly than human Ab<sup>95,96</sup>. However, it was reported that single mutations for Y10 and H13 promote Ab aggregation<sup>95,97</sup>. Therefore, the mutation of Arg5 is important in suppressing Ab aggregation, as shown in our study. Additionally, the English (H6R) and Tottori (D7N) mutations are associated with familial AD. They are known as mutations that accelerate the Ab aggregation. Since these mutations increase the positive charges or decrease the negative charges in the region near residue 5, they are essential for Ab42 to form a b-hairpin (Fig. 7). For Ab40, Ab40 molecules may easily form intermolecular contacts due to an increase in the positive charge in the N-terminal region. As mentioned in the previous subsection, such intermolecular contacts in the N-terminal region are essential for Ab oligomerization.

## Conclusions

It is known that Ab42 forms oligomers more rapidly than Ab40. To investigate the role of the two additional C-terminal residues of Ab42 in accelerating the oligomer formation, we performed the Coulomb replica-permutation molecular dynamics (CRPMD) simulation for two Ab42 molecules in explicit water. We also conducted the CRPMD simulation for two Ab40 molecules to clarify the difference in oligomerization processes between Ab42 and Ab40.

We showed that the probability of the dimer formation for Ab42 was slightly higher than that of Ab40. In the dimer structures for both Ab systems, the b1 and b2 regions tended to form the intermolecular antiparallel b-sheets. Additionally, we obtained that the Ab42 dimer forms the stable intermolecular b-sheet with the longer b-strands than the Ab40 dimer. For the intramolecular structures, Ab42 formed the b-hairpin with a higher probability than Ab40. The b-hairpin formation is essential in forming the stable intermolecular b-sheet. In fact, more intermolecular b-bridges were formed with more intramolecular b-bridges in both Abs.

Ab42 forms more b-hairpin because of the following reasons. The contacts between the C-terminus and Arg5 and between E22 and K28 are maintained by their electrostatic interactions in Ab42. Due to these contacts, the distance between the b1 and b2 regions is inevitably shortened. The region from Arg5 to E22 and that from K28 to A42 have almost the same number of residues. These regions can have extended structures simultaneously. The b-hairpin can easily be formed between these close extended structures. To see whether Arg5 is needed to stabilize the b-hairpin, we performed additional molecular dynamics (MD) simulations of the wild type and mutants (R5G and R5E). Consequently, the b-hairpin was maintained in the wild type; however, it was gradually broken in the mutants.

These simulation results show that Arg5 plays an essential role in the Ab42 aggregation. We conducted the experiments on Ab aggregations to confirm the accuracy of the prediction from the simulation. The experimental results show that the mutation of Arg5 suppresses the Ab42 aggregation. We also obtained that the Arg5 mutation suppresses not only the Ab42 aggregation but also the Ab40 aggregation. The MD simulations elucidated that Arg5 is essential for the intramolecular contact in Ab42, whereas it is essential for the intermolecular contact in Ab40.

In this study, we have successfully identified the key residue, Arg5, for the Ab42 and Ab40 oligomerizations. For the Ab42 oligomerization, we predicted this key residue prior to the experiments using the Hamiltonian replica-permutation method. This shows that MD simulation with efficient conformational sampling is useful for elucidating oligomerization processes of proteins. By performing the MD simulations and experiments, we obtained that the key residue plays different roles in the Ab42 and Ab40 oligomerizations. Such a collaborative approach between simulation and experiments is essential in understanding protein oligomerization. Through the simulations, we investigated dimerization, which is the smallest unit of oligomerization. Consequently, we obtained that there is a difference between Ab42 and Ab40. The fact that we could predict the experimental results from the simulation results means that the differences seen in the formation of dimers make a difference in the

formation of much larger aggregates, such as amyloid fibrils observed in experiments. Thus, it is essential to elucidate the process of small oligomer formation to fully understand the Ab aggregation.

## Declarations

### Acknowledgements

This work used supercomputers at the Research Center for Computational Science, Okazaki Research Facilities, National Institutes of Natural Sciences and the Supercomputer Center, the Institute for Solid State Physics, the University of Tokyo. This work was supported by JSPS KAKENHI Grant Number JP21K06040, JP16K18531, JP19K07041, and JP21K06118. This work was also supported by the ExCELLS Research for Young Scientists.

### Author contributions

S. G. I. and H. O. designed the research. S. G. I. modeled the initial conformations, performed simulations, and analyzed the simulation results. M. Y.-U. and K. K. prepared samples and conducted experiments. S. G. I. and M. Y.-U. wrote the paper. All authors discussed the results and revised the paper.

### Competing interests

The authors declare no competing interests.

### Additional information

**Supplementary information.** Description of CRPM, preparation of the initial conformations for the CRPMD simulations and for the MD simulations of the Ab monomers, and details of PCA (PDF). Movies S1–S3 (AVI).

## References

1. Chiti F, Dobson CM. Protein misfolding, functional amyloid, and human disease. *Annu Rev Biochem* **75**, 333–366 (2006).
2. Chiti F, Dobson CM. Protein Misfolding, Amyloid Formation, and Human Disease: A Summary of Progress Over the Last Decade. *Annu Rev Biochem* **86**, 27–68 (2017).
3. Iadanza MG, Jackson MP, Hewitt EW, Ranson NA, Radford SE. A new era for understanding amyloid structures and disease. *Nat. Rev. Mol. Cell Biol.* **19**, 755–773 (2018).
4. Picken MM. The Pathology of Amyloidosis in Classification: A Review. *Acta Haematol* **143**, 322–334 (2020).
5. Sipe JD. Amyloidosis. *Annu Rev Biochem* **61**, 947–975 (1992).
6. Hayden EY, Teplow DB. Amyloid beta-protein oligomers and Alzheimer's disease. *Alzheimers Res Ther* **5**, 60 (2013).

7. Kirschner DA, Abraham C, Selkoe DJ. X-ray diffraction from intraneuronal paired helical filaments and extraneuronal amyloid fibers in Alzheimer disease indicates cross-beta conformation. *Proc Natl Acad Sci U S A* **83**, 503–507 (1986).
8. Inouye H, Fraser PE, Kirschner DA. Structure of beta-crystallite assemblies formed by Alzheimer beta-amyloid protein analogues: analysis by x-ray diffraction. *Biophys. J.* **64**, 502–519 (1993).
9. Paravastu AK, Leapman RD, Yau WM, Tycko R. Molecular structural basis for polymorphism in Alzheimer's beta-amyloid fibrils. *Proc Natl Acad Sci U S A* **105**, 18349–18354 (2008).
10. Xiao Y, *et al.* Aβ(1-42) fibril structure illuminates self-recognition and replication of amyloid in Alzheimer's disease. *Nat. Struct. Mol. Biol.* **22**, 499–505 (2015).
11. Colvin MT, *et al.* Atomic Resolution Structure of Monomorphic Aβ42 Amyloid Fibrils. *J. Am. Chem. Soc.* **138**, 9663–9674 (2016).
12. Luhrs T, *et al.* 3D structure of Alzheimer's amyloid-beta(1-42) fibrils. *Proc Natl Acad Sci U S A* **102**, 17342–17347 (2005).
13. Gremer L, *et al.* Fibril structure of amyloid-beta(1-42) by cryo-electron microscopy. *Science* **358**, 116–119 (2017).
14. Schmidt M, *et al.* Peptide dimer structure in an Aβ(1-42) fibril visualized with cryo-EM. *Proc Natl Acad Sci U S A* **112**, 11858–11863 (2015).
15. Yu L, *et al.* Structural characterization of a soluble amyloid beta-peptide oligomer. *Biochemistry* **48**, 1870–1877 (2009).
16. Sarkar B, *et al.* Significant structural differences between transient amyloid-beta oligomers and less-toxic fibrils in regions known to harbor familial Alzheimer's mutations. *Angew. Chem. Int. Ed. Engl.* **53**, 6888–6892 (2014).
17. Kang J, *et al.* The precursor of Alzheimer's disease amyloid A4 protein resembles a cell-surface receptor. *Nature* **325**, 733–736 (1987).
18. Jakob-Roetne R, Jacobsen H. Alzheimer's disease: from pathology to therapeutic approaches. *Angew. Chem. Int. Ed. Engl.* **48**, 3030–3059 (2009).
19. Zheng L, Cedazo-Minguez A, Hallbeck M, Jerhammar F, Marcusson J, Terman A. Intracellular distribution of amyloid beta peptide and its relationship to the lysosomal system. *Transl Neurodegener* **1**, 19 (2012).
20. Klein AM, Kowall NW, Ferrante RJ. Neurotoxicity and oxidative damage of beta amyloid 1-42 versus beta amyloid 1-40 in the mouse cerebral cortex. *Ann. N. Y. Acad. Sci.* **893**, 314–320 (1999).
21. Miller DL, *et al.* Peptide compositions of the cerebrovascular and senile plaque core amyloid deposits of Alzheimer's disease. *Arch. Biochem. Biophys.* **301**, 41–52 (1993).
22. Iwatsubo T, Odaka A, Suzuki N, Mizusawa H, Nukina N, Ihara Y. Visualization of Aβ42(43) and Aβ40 in senile plaques with end-specific Aβ monoclonals: Evidence that an initially deposited species is Aβ42(43). *Neuron* **13**, 45–53 (1994).

23. Gravina SA, *et al.* Amyloid beta protein (A beta) in Alzheimer's disease brain. Biochemical and immunocytochemical analysis with antibodies specific for forms ending at A beta 40 or A beta 42(43). *J. Biol. Chem.* **270**, 7013–7016 (1995).
24. Borchelt DR, *et al.* Familial Alzheimer's disease-linked presenilin 1 variants elevate Abeta1-42/1-40 ratio in vitro and in vivo. *Neuron* **17**, 1005–1013 (1996).
25. Kumar-Singh S, *et al.* Mean age-of-onset of familial alzheimer disease caused by presenilin mutations correlates with both increased Abeta42 and decreased Abeta40. *Hum. Mutat.* **27**, 686–695 (2006).
26. Baldassarre M, Baronio CM, Morozova-Roche LA, Barth A. Amyloid beta-peptides 1-40 and 1-42 form oligomers with mixed beta-sheets. *Chem Sci* **8**, 8247–8254 (2017).
27. Bi C, Bi S, Li B. Processing of Mutant beta-Amyloid Precursor Protein and the Clinicopathological Features of Familial Alzheimer's Disease. *Aging Dis* **10**, 383–403 (2019).
28. Jarrett JT, Berger EP, Lansbury PT, Jr. The carboxy terminus of the beta amyloid protein is critical for the seeding of amyloid formation: implications for the pathogenesis of Alzheimer's disease. *Biochemistry* **32**, 4693–4697 (1993).
29. El-Agnaf OM, Mahil DS, Patel BP, Austen BM. Oligomerization and toxicity of beta-amyloid-42 implicated in Alzheimer's disease. *Biochem. Biophys. Res. Commun.* **273**, 1003–1007 (2000).
30. Sgourakis NG, *et al.* Atomic-Level Characterization of the Ensemble of the A $\beta$ (1–42) Monomer in Water Using Unbiased Molecular Dynamics Simulations and Spectral Algorithms. *J. Mol. Biol.* **405**, 570 (2011).
31. Velez-Vega C, Escobedo FA. Characterizing the structural behavior of selected Abeta-42 monomers with different solubilities. *J. Phys. Chem. B* **115**, 4900–4910 (2011).
32. Olubiyi OO, Strodel B. Structures of the Amyloid  $\beta$ -Peptides. A $\beta$ 1–40 and A $\beta$ 1–42 as Influenced by pH and a d-Peptide. *J. Phys. Chem. B* **116**, 3280 (2012).
33. Rosenman DJ, Connors CR, Chen W, Wang C, Garcia AE. A $\beta$  Monomers Transiently Sample Oligomer and Fibril-Like Configurations: Ensemble Characterization Using a Combined MD/NMR Approach. *J. Mol. Biol.* **425**, 3338 (2013).
34. Rosenman DJ, Wang C, Garcia AE. Characterization of A $\beta$  Monomers through the Convergence of Ensemble Properties among Simulations with Multiple Force Fields. *J. Phys. Chem. B* **120**, 259 (2016).
35. Itoh SG, Yagi-Utsumi M, Kato K, Okumura H. Effects of a Hydrophilic/Hydrophobic Interface on Amyloid-beta Peptides Studied by Molecular Dynamics Simulations and NMR Experiments. *J. Phys. Chem. B* **123**, 160–169 (2019).
36. O'Brien EP, Okamoto Y, Straub JE, Brooks BR, Thirumalai D. Thermodynamic perspective on the dock-lock growth mechanism of amyloid fibrils. *J. Phys. Chem. B* **113**, 14421–14430 (2009).
37. Straub JE, Thirumalai D. Toward a molecular theory of early and late events in monomer to amyloid fibril formation. *Annu. Rev. Phys. Chem.* **62**, 437–463 (2011).

38. Schwierz N, Frost CV, Geissler PL, Zacharias M. Dynamics of Seeded Abeta40-Fibril Growth from Atomistic Molecular Dynamics Simulations: Kinetic Trapping and Reduced Water Mobility in the Locking Step. *J. Am. Chem. Soc.* **138**, 527–539 (2016).
39. Sasmal S, Schwierz N, Head-Gordon T. Mechanism of Nucleation and Growth of Abeta40 Fibrils from All-Atom and Coarse-Grained Simulations. *J. Phys. Chem. B* **120**, 12088–12097 (2016).
40. Bacci M, Vymetal J, Mihajlovic M, Caflisch A, Vitalis A. Amyloid  $\beta$  Fibril Elongation by Monomers Involves Disorder at the Tip. *J. Chem. Theory Comput.* **13**, 5117 (2017).
41. Buchete NV, Tycko R, Hummer G. Molecular dynamics simulations of Alzheimer's beta-amyloid protofilaments. *J. Mol. Biol.* **353**, 804–821 (2005).
42. Baumketner A, Krone MG, Shea JE. Role of the familial Dutch mutation E22Q in the folding and aggregation of the 15-28 fragment of the Alzheimer amyloid-beta protein. *Proc Natl Acad Sci U S A* **105**, 6027–6032 (2008).
43. Lemkul JA, Bevan DR. Assessing the stability of Alzheimer's amyloid protofibrils using molecular dynamics. *J. Phys. Chem. B* **114**, 1652–1660 (2010).
44. Okumura H, Itoh SG. Structural and Fluctuational Difference Between Two Ends of A $\beta$  Amyloid Fibril: MD Simulations Predict Only One End has Open Conformations. *Sci. Rep.* **106**, 38422 (2016).
45. Rodriguez RA, Chen LY, Plascencia-Villa G, Perry G. Thermodynamics of Amyloid-beta Fibril Elongation: Atomistic Details of the Transition State. *ACS Chem Neurosci* **9**, 783–789 (2018).
46. Davidson DS, Brown AM, Lemkul JA. Insights into Stabilizing Forces in Amyloid Fibrils of Differing Sizes from Polarizable Molecular Dynamics Simulations. *J. Mol. Biol.* **430**, 3819–3834 (2018).
47. Ilie IM, Caflisch A. Disorder at the Tips of a Disease-Relevant A $\beta$ 42 Amyloid Fibril: A Molecular Dynamics Study. *J. Phys. Chem. B* **122**, 11072 (2018).
48. Okumura H, Itoh SG. Amyloid fibril disruption by ultrasonic cavitation: nonequilibrium molecular dynamics simulations. *J. Am. Chem. Soc.* **136**, 10549–10552 (2014).
49. Hoang Viet M, Derreumaux P, Nguyen PH. Nonequilibrium all-atom molecular dynamics simulation of the bubble cavitation and application to dissociate amyloid fibrils. *J. Chem. Phys.* **145**, 174113 (2016).
50. Hoang Viet M, Derreumaux P, Li MS, Roland C, Sagui C, Nguyen PH. Picosecond dissociation of amyloid fibrils with infrared laser: A nonequilibrium simulation study. *J. Chem. Phys.* **143**, 155101 (2015).
51. Okumura H, Itoh SG, Nakamura K, Kawasaki T. Role of Water Molecules and Helix Structure Stabilization in the Laser-Induced Disruption of Amyloid Fibrils Observed by Nonequilibrium Molecular Dynamics Simulations. *J. Phys. Chem. B* **125**, 4964–4976 (2021).
52. Nguyen PH, Li MS, Stock G, Straub JE, Thirumalai D. Monomer adds to preformed structured oligomers of Abeta-peptides by a two-stage dock-lock mechanism. *Proc Natl Acad Sci U S A* **104**, 111–116 (2007).

53. Klimov DK, Thirumalai D. Dissecting the Assembly of A $\beta$ 16–22 Amyloid Peptides into Antiparallel  $\beta$  Sheets. *Structure* **11**, 295–307 (2003).
54. Hwang W, Zhang S, Kamm RD, Karplus M. Kinetic control of dimer structure formation in amyloid fibrillogenesis. *Proc Natl Acad Sci U S A* **101**, 12916–12921 (2004).
55. Gnanakaran S, Nussinov R, Garcia AE. Atomic-level description of amyloid beta-dimer formation. *J. Am. Chem. Soc.* **128**, 2158–2159 (2006).
56. Nguyen PH, Li MS, Derreumaux P. Effects of all-atom force fields on amyloid oligomerization: replica exchange molecular dynamics simulations of the Abeta(16-22) dimer and trimer. *Phys. Chem. Chem. Phys.* **13**, 9778–9788 (2011).
57. Okumura H, Itoh SG. Molecular dynamics simulations of amyloid-beta(16-22) peptide aggregation at air-water interfaces. *J. Chem. Phys.* **152**, 095101 (2020).
58. Ngoc LLN, Itoh SG, Sompornpisut P, Okumura H. Replica-permutation molecular dynamics simulations of an amyloid- $\beta$ (16–22) peptide and polyphenols. *Chem. Phys. Lett.* **758**, 137913 (2020).
59. Tarus B, Straub JE, Thirumalai D. Probing the initial stage of aggregation of the Abeta(10-35)-protein: assessing the propensity for peptide dimerization. *J. Mol. Biol.* **345**, 1141–1156 (2005).
60. Itoh SG, Okamoto Y. Amyloid-beta(29-42) dimer formations studied by a multicanonical-multioverlap molecular dynamics simulation. *J. Phys. Chem. B* **112**, 2767–2770 (2008).
61. Lu Y, Wei G, Derreumaux P. Effects of G33A and G33I mutations on the structures of monomer and dimer of the amyloid-beta fragment 29-42 by replica exchange molecular dynamics simulations. *J. Phys. Chem. B* **115**, 1282–1288 (2011).
62. Itoh SG, Okumura H. Dimerization process of amyloid-beta(29-42) studied by the Hamiltonian replica-permutation molecular dynamics simulations. *J. Phys. Chem. B* **118**, 11428–11436 (2014).
63. Itoh SG, Okumura H. Oligomer Formation of Amyloid-beta(29-42) from Its Monomers Using the Hamiltonian Replica-Permutation Molecular Dynamics Simulation. *J. Phys. Chem. B* **120**, 6555–6561 (2016).
64. Tarus B, Tran TT, Nasica-Labouze J, Sterpone F, Nguyen PH, Derreumaux P. Structures of the Alzheimer's Wild-Type Abeta1-40 Dimer from Atomistic Simulations. *J. Phys. Chem. B* **119**, 10478–10487 (2015).
65. Man VH, Nguyen PH, Derreumaux P. Conformational Ensembles of the Wild-Type and S8C Abeta1-42 Dimers. *J. Phys. Chem. B* **121**, 2434–2442 (2017).
66. Ilie IM, Caflisch A. Simulation Studies of Amyloidogenic Polypeptides and Their Aggregates. *Chem Rev* **119**, 6956–6993 (2019).
67. Hukushima K, Nemoto K. Exchange Monte Carlo method and application to spin glass simulations. *J. Phys. Soc. Jpn.* **65**, 1604–1608 (1996).
68. Sugita Y, Okamoto Y. Replica-exchange molecular dynamics method for protein folding. *Chem. Phys. Lett.* **314**, 141–151 (1999).

69. Itoh SG, Okumura H. Replica-Permutation Method with the Suwa-Todo Algorithm beyond the Replica-Exchange Method. *J Chem Theory Comput* **9**, 570–581 (2013).
70. Metropolis N, Rosenbluth AW, Rosenbluth MN, Teller AH, Teller E. Equation of State Calculations by Fast Computing Machines. *The Journal of Chemical Physics* **21**, 1087–1092 (1953).
71. Suwa H, Todo S. Markov chain Monte Carlo method without detailed balance. *Phys. Rev. Lett.* **105**, 120603 (2010).
72. Itoh SG, Okumura H. Hamiltonian replica-permutation method and its applications to an alanine dipeptide and amyloid-beta(29-42) peptides. *J. Comput. Chem.* **34**, 2493–2497 (2013).
73. Hornak V, Abel R, Okur A, Strockbine B, Roitberg A, Simmerling C. Comparison of multiple Amber force fields and development of improved protein backbone parameters. *Proteins* **65**, 712–725 (2006).
74. Jorgensen WL, Chandrasekhar J, Madura JD, Impey RW, Klein ML. Comparison of simple potential functions for simulating liquid water. *The Journal of Chemical Physics* **79**, 926–935 (1983).
75. Darden T, York D, Pedersen L. Particle Mesh Ewald - an N.Log(N) Method for Ewald Sums in Large Systems. *J. Chem. Phys.* **98**, 10089–10092 (1993).
76. Nosé S. A molecular dynamics method for simulations in the canonical ensemble. *Journal Molecular Physics* **52**, 255–268 (1984).
77. Nosé S. A unified formulation of the constant temperature molecular dynamics methods. *The Journal of Chemical Physics* **81**, 511–519 (1984).
78. Hoover WG. Canonical dynamics: Equilibrium phase-space distributions. *Phys Rev A Gen Phys* **31**, 1695–1697 (1985).
79. Okumura H, Itoh SG, Okamoto Y. Explicit symplectic integrators of molecular dynamics algorithms for rigid-body molecules in the canonical, isobaric-isothermal, and related ensembles. *J. Chem. Phys.* **126**, 084103 (2007).
80. Allen MP, Tildesley DJ. *Computer Simulation of Liquids: Second Edition*, 2 edn. Oxford University Press (2017).
81. Ferrenberg AM, Swendsen RH. Optimized Monte Carlo data analysis. *Phys. Rev. Lett.* **63**, 1195–1198 (1989).
82. Kumar S, Rosenberg JM, Bouzida D, Swendsen RH, Kollman PA. THE weighted histogram analysis method for free-energy calculations on biomolecules. I. The method. *J. Comput. Chem.* **13**, 1011–1021 (1992).
83. Berg BA. *Markov Chain Monte Carlo Simulations and Their Statistical Analysis*. WORLD SCIENTIFIC (2004).
84. Kabsch W, Sander C. Dictionary of protein secondary structure: pattern recognition of hydrogen-bonded and geometrical features. *Biopolymers* **22**, 2577–2637 (1983).
85. Bitan G, Kirkitadze MD, Lomakin A, Vollers SS, Benedek GB, Teplow DB. Amyloid beta -protein (A $\beta$ ) assembly: A $\beta$  40 and A $\beta$  42 oligomerize through distinct pathways. *Proc Natl Acad Sci U S A*

- 100, 330–335 (2003).
86. Abelein A, *et al.* The hairpin conformation of the amyloid beta peptide is an important structural motif along the aggregation pathway. *J. Biol. Inorg. Chem.* **19**, 623–634 (2014).
  87. Maity S, Hashemi M, Lyubchenko YL. Nano-assembly of amyloid beta peptide: role of the hairpin fold. *Sci Rep* **7**, 2344 (2017).
  88. Chiang HL, Chen CJ, Okumura H, Hu CK. Transformation between alpha-helix and beta-sheet structures of one and two polyglutamine peptides in explicit water molecules by replica-exchange molecular dynamics simulations. *J. Comput. Chem.* **35**, 1430–1437 (2014).
  89. Araki M, Tamura A. Transformation of an alpha-helix peptide into a beta-hairpin induced by addition of a fragment results in creation of a coexisting state. *Proteins* **66**, 860–868 (2007).
  90. Itoh SG, Tamura A, Okamoto Y. Helix-Hairpin Transitions of a Designed Peptide Studied by a Generalized-Ensemble Simulation. *Journal of Chemical Theory and Computation* **6**, 979–983 (2010).
  91. Okumura H, Itoh SG. Transformation of a design peptide between the alpha-helix and beta-hairpin structures using a helix-strand replica-exchange molecular dynamics simulation. *Phys. Chem. Chem. Phys.* **15**, 13852–13861 (2013).
  92. Chakraborty D, Chebaro Y, Wales DJ. A multifunnel energy landscape encodes the competing alpha-helix and beta-hairpin conformations for a designed peptide. *Phys. Chem. Chem. Phys.* **22**, 1359–1370 (2020).
  93. Karplus M, Kushick JN. Method for Estimating the Configurational Entropy of Macromolecules. *Macromolecules* **14**, 325–332 (1981).
  94. De Strooper B, Simons M, Multhaup G, Van Leuven F, Beyreuther K, Dotti CG. Production of intracellular amyloid-containing fragments in hippocampal neurons expressing human amyloid precursor protein and protection against amyloidogenesis by subtle amino acid substitutions in the rodent sequence. *EMBO J.* **14**, 4932–4938 (1995).
  95. Poduslo JF, *et al.* HH domain of Alzheimer's disease Aβ provides structural basis for neuronal binding in PC12 and mouse cortical/hippocampal neurons. *PLoS One* **5**, e8813 (2010).
  96. Foroutanpay BV, *et al.* The Effects of N-terminal Mutations on beta-amyloid Peptide Aggregation and Toxicity. *Neuroscience* **379**, 177–188 (2018).
  97. Dai X, *et al.* Aβ40 Y10F increases beta-fibrils formation but attenuates the neurotoxicity of amyloid-beta peptide. *Int J Mol Sci* **13**, 5324–5337 (2012).

## Figures

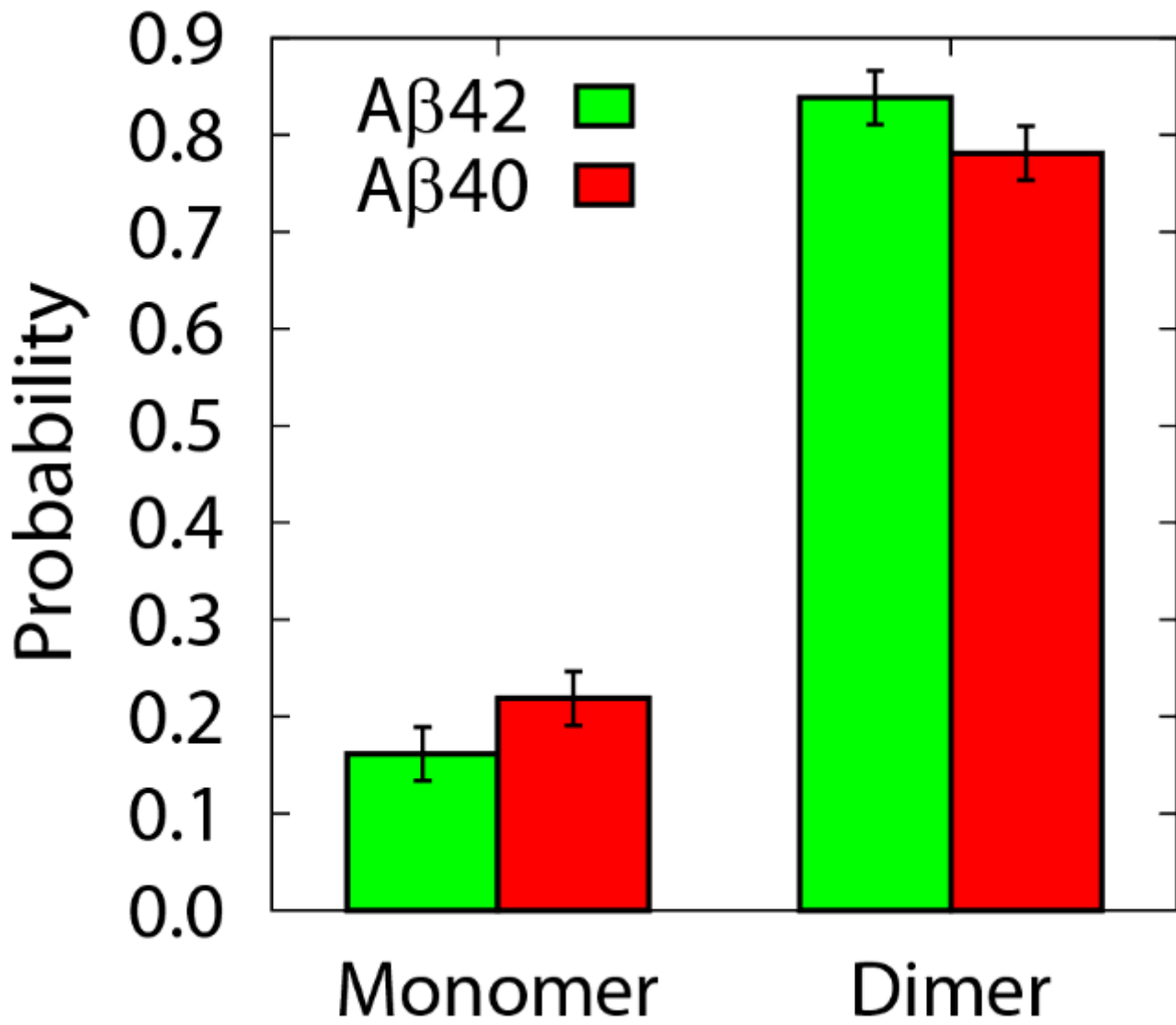
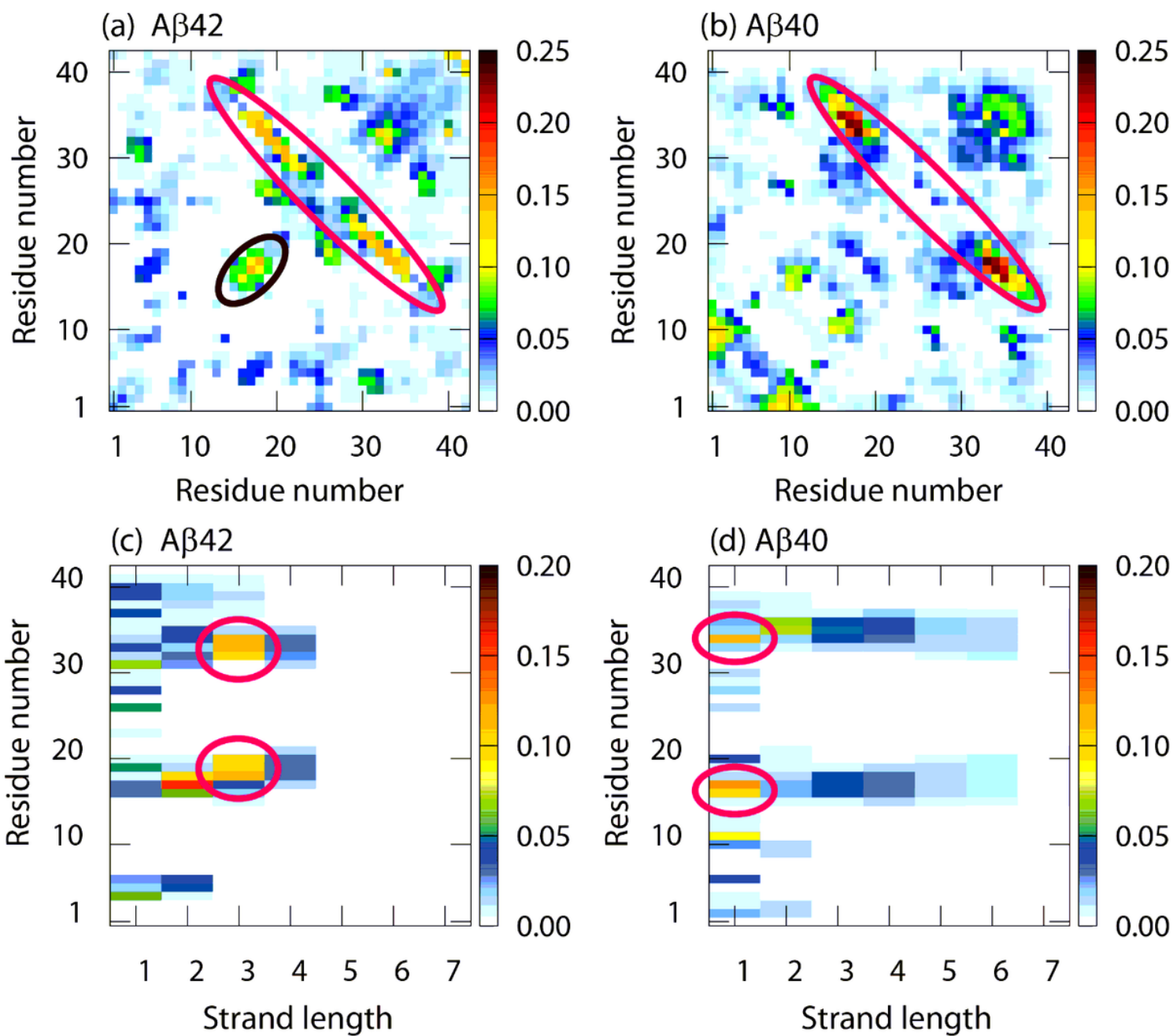


Figure 1

Distributions of oligomer sizes for Ab42 (green) and Ab40 (red).



**Figure 2**

Intermolecular contact probabilities of  $C_a$  atoms for (a) Ab42 and (b) Ab40. Probabilities with which the residues in (c) Ab42 and (d) Ab40 form b-strands with the corresponding length.

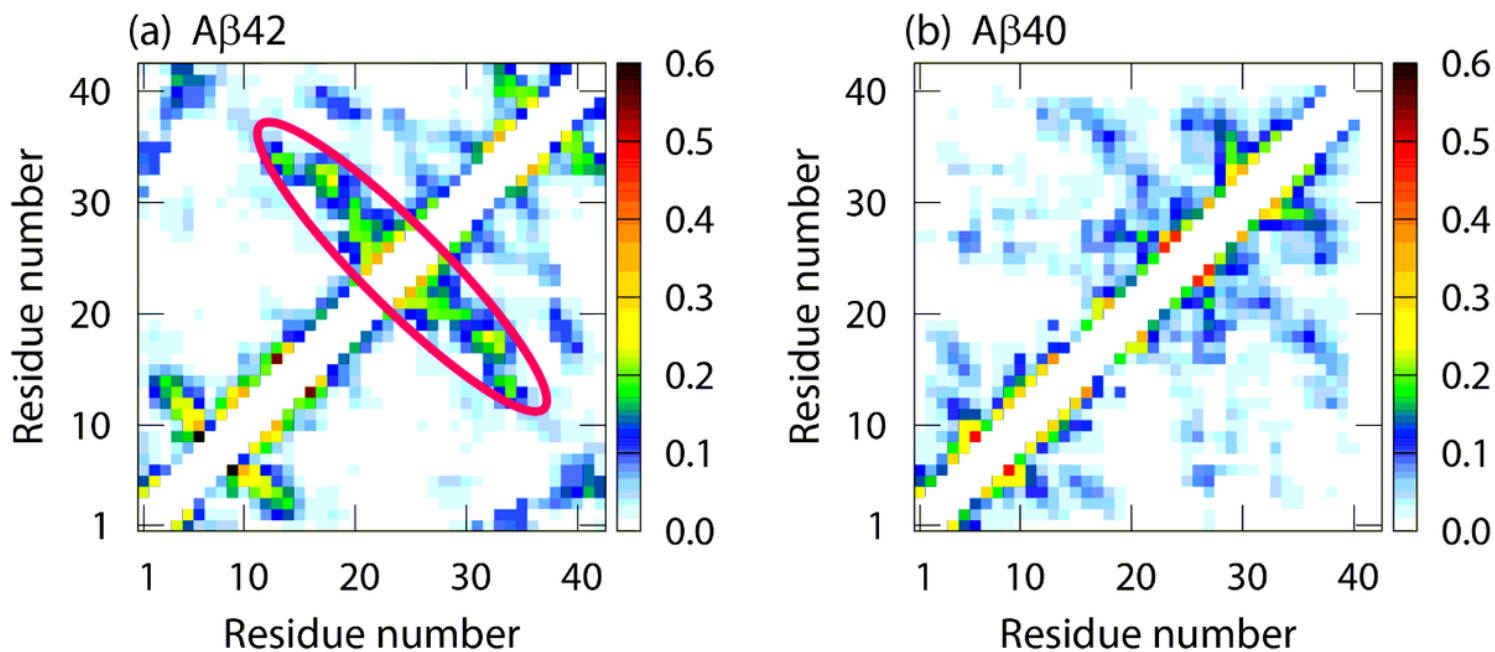


**Figure 3**

Intramolecular contact probabilities of  $C_{\alpha}$  atoms for (a) Ab42 and (b) Ab40.

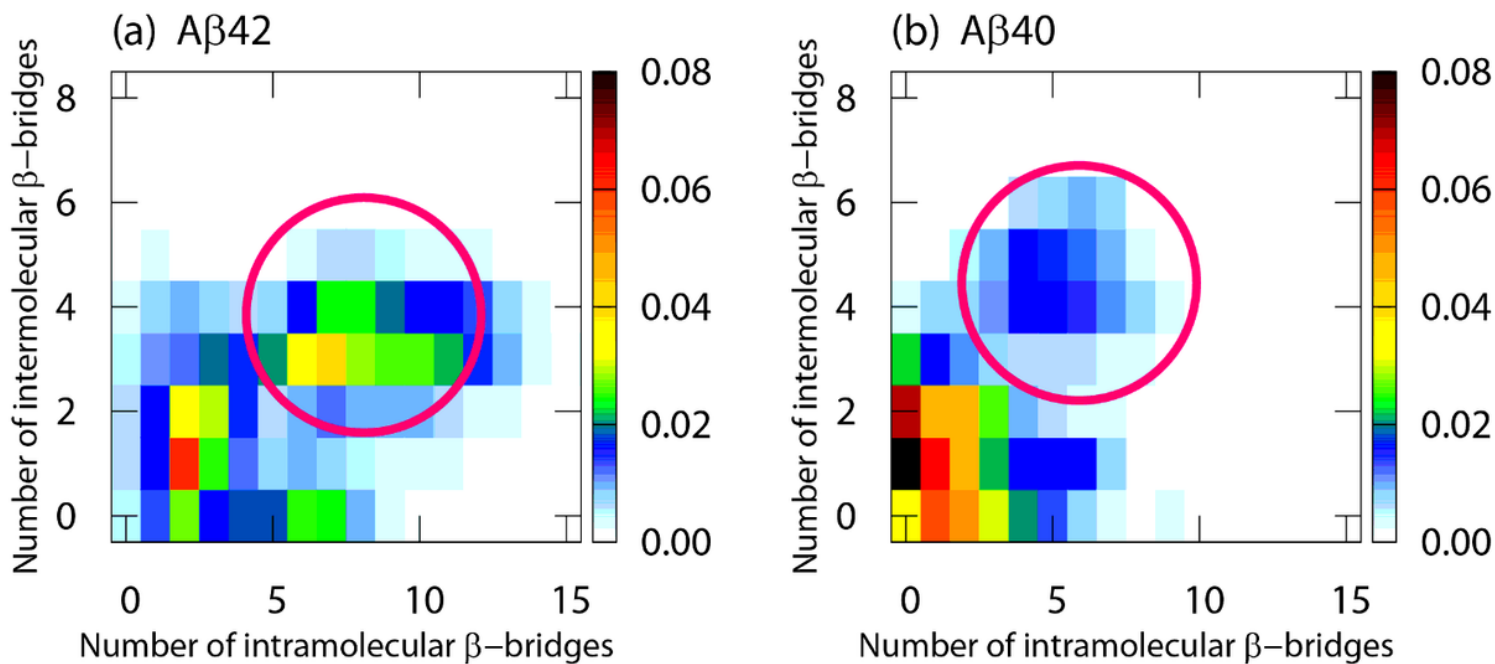


**Figure 4**

Probability distributions with respect to the number of intramolecular and intermolecular  $\beta$ -bridges for (a) Ab42 and (b) Ab40.

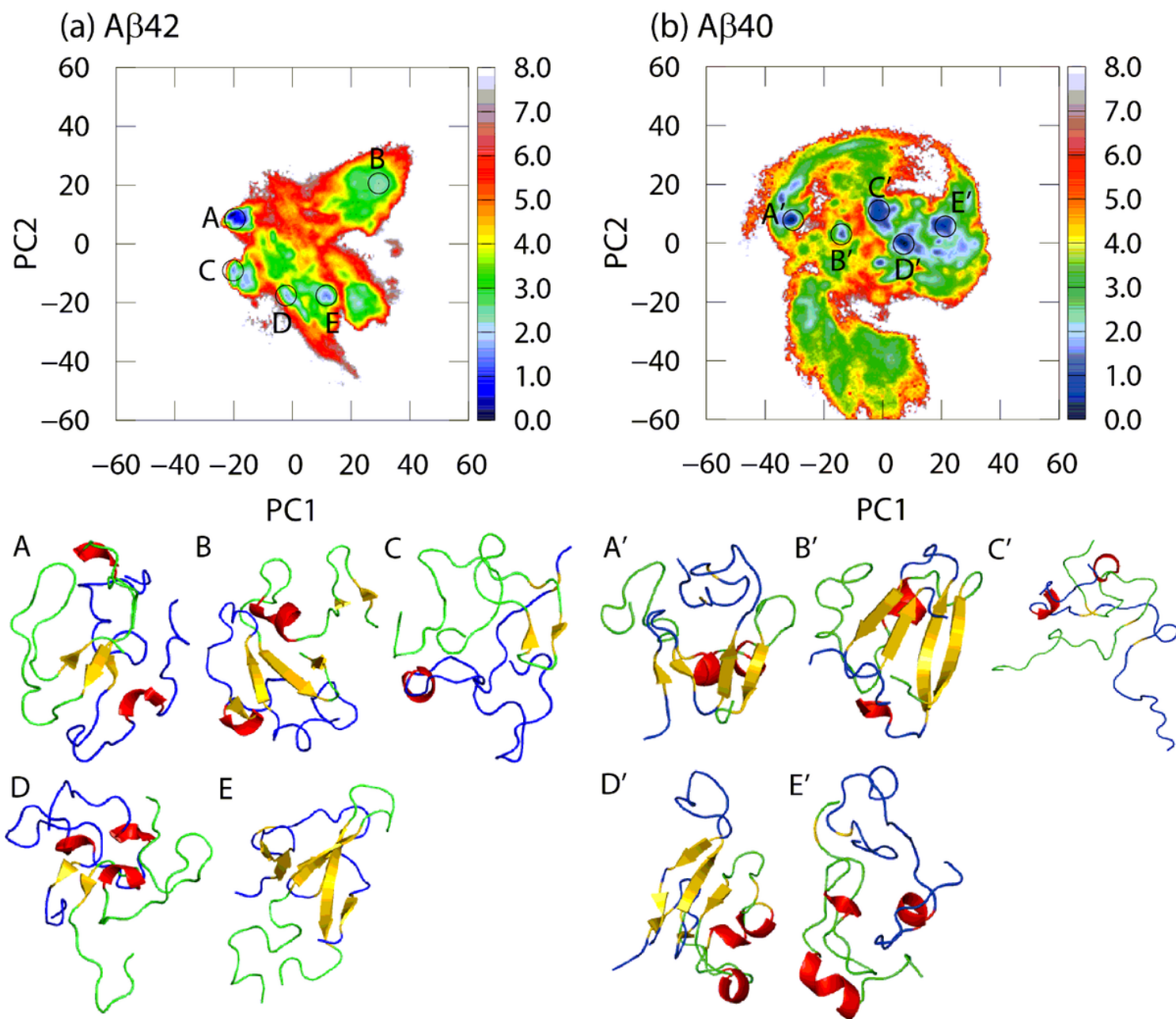


**Figure 5**

Free-energy landscapes for (a) Aβ42 and (b) Aβ40 with respect to the corresponding first and second principal components (PC1 and PC2). The local-minimum free-energy states are labeled as (a) states A–E for Aβ42 and (b) states A'–E' for Aβ40. The units of the free-energy landscapes are kcal/mol. Representative dimer structures in (a) states A–E and (b) states A'–E' are also shown.

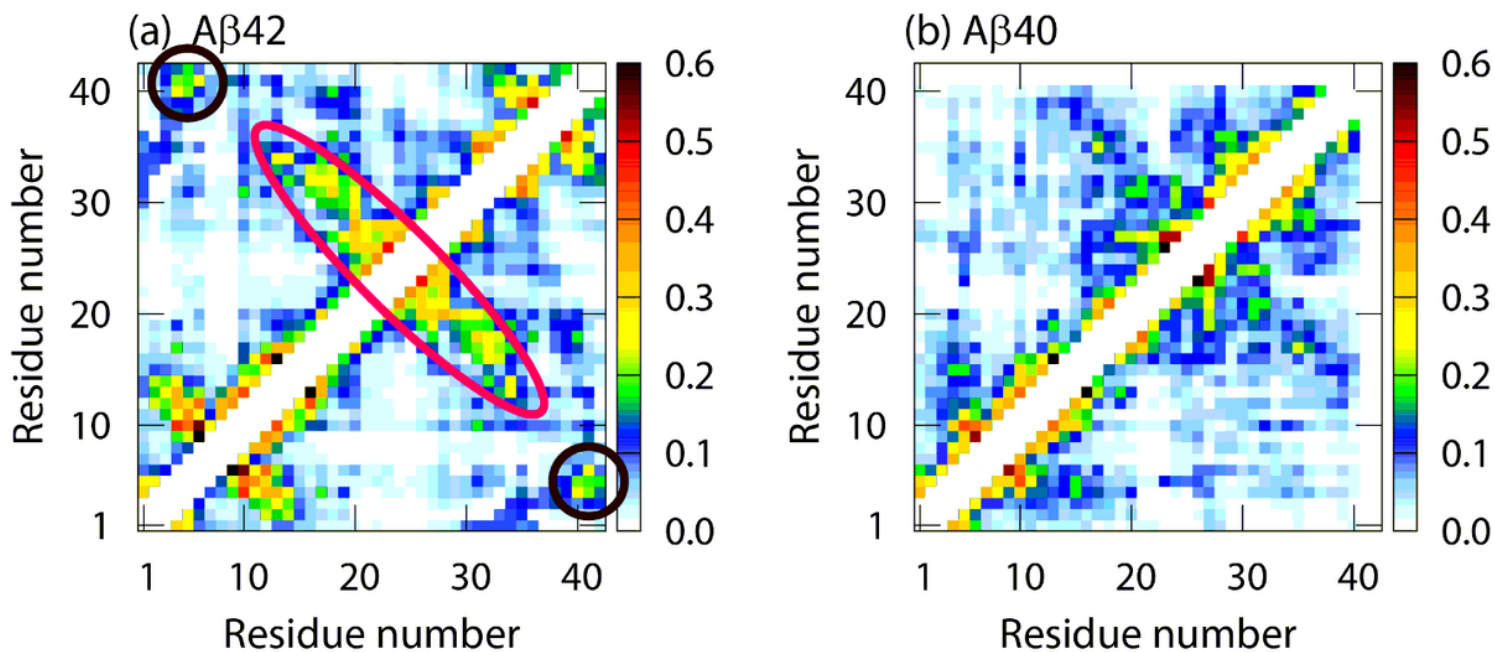


Figure 6

Intramolecular contact probabilities between residues for (a) Ab42 and (b) Ab40. Here, all atoms, including the sidechain atoms, except the hydrogen atoms, are considered in calculating the contact probabilities.

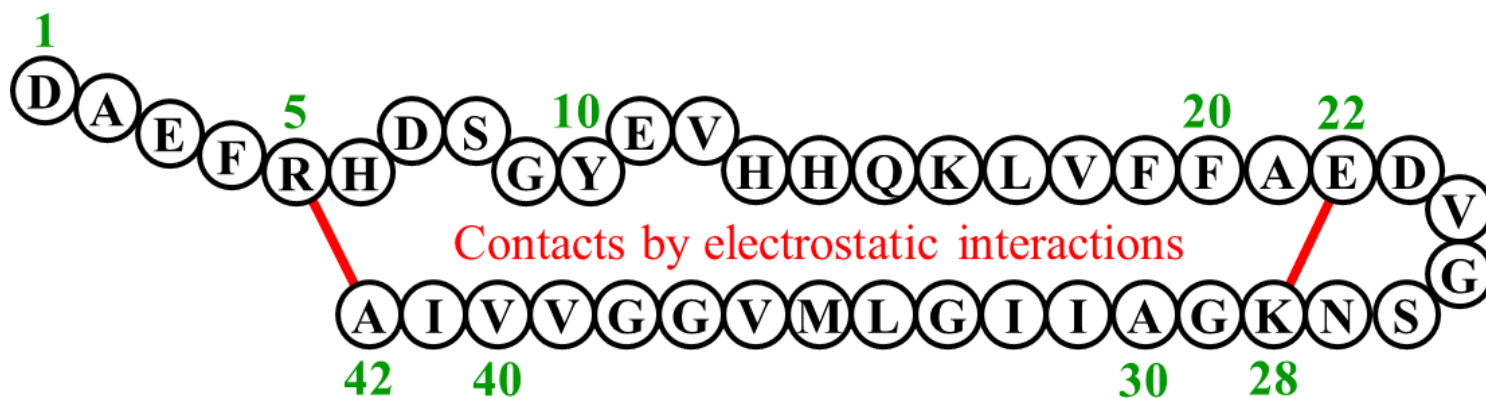
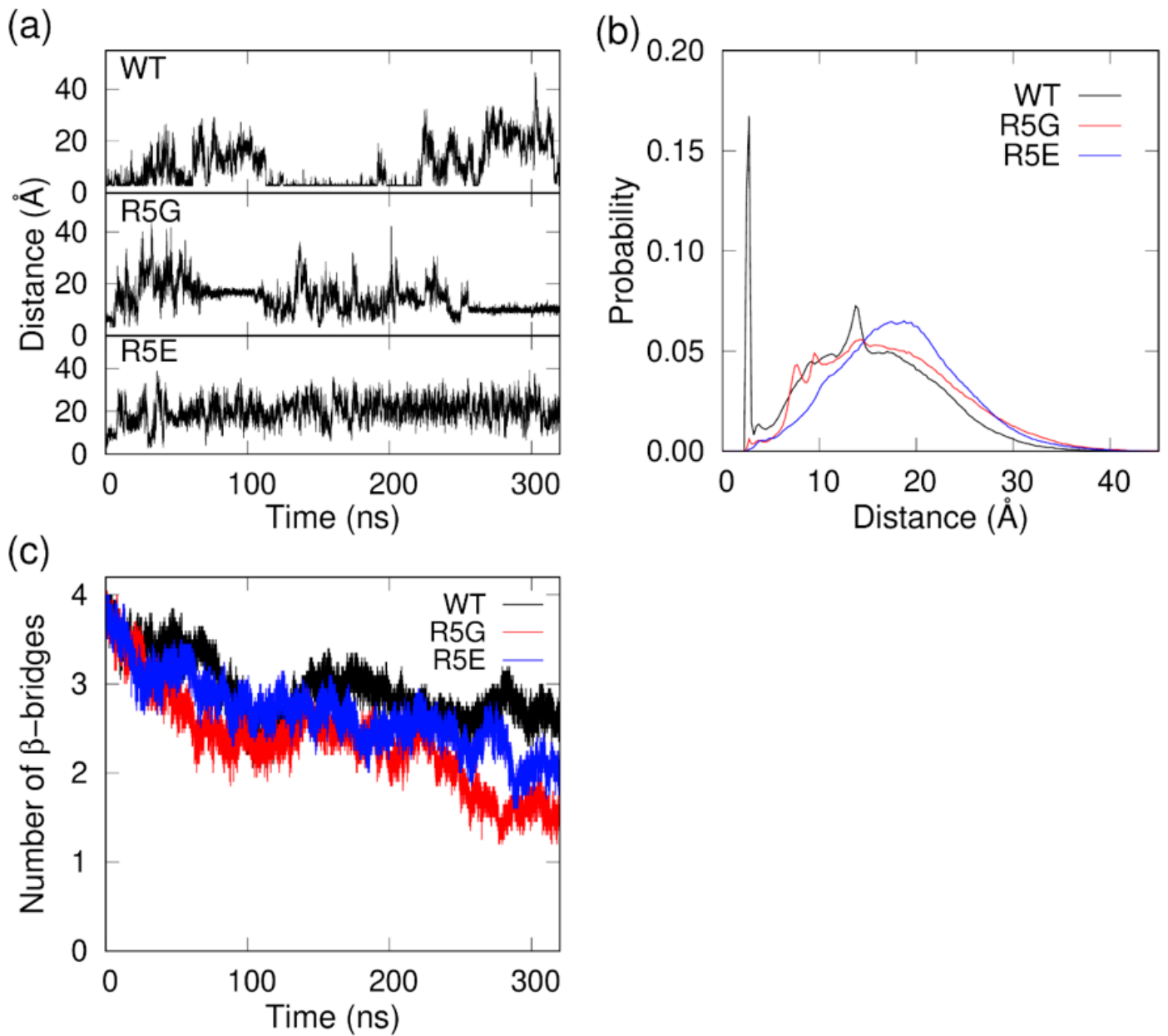


Figure 7

Schematic illustration where the b-hairpin of Ab42 is stabilized by the contacts between the C-terminus and Arg5 and between E22 and K28.



**Figure 8**

(a) Time series of distances between residue 5 and C-terminal residue for the wild type and mutants. (b) Probability distributions of distances between residue 5 and C-terminal residue for the wild type and mutants. (c) Time series of the average numbers of  $\beta$ -bridges between the b1 and b2 regions calculated from 20 MD simulations for each system.

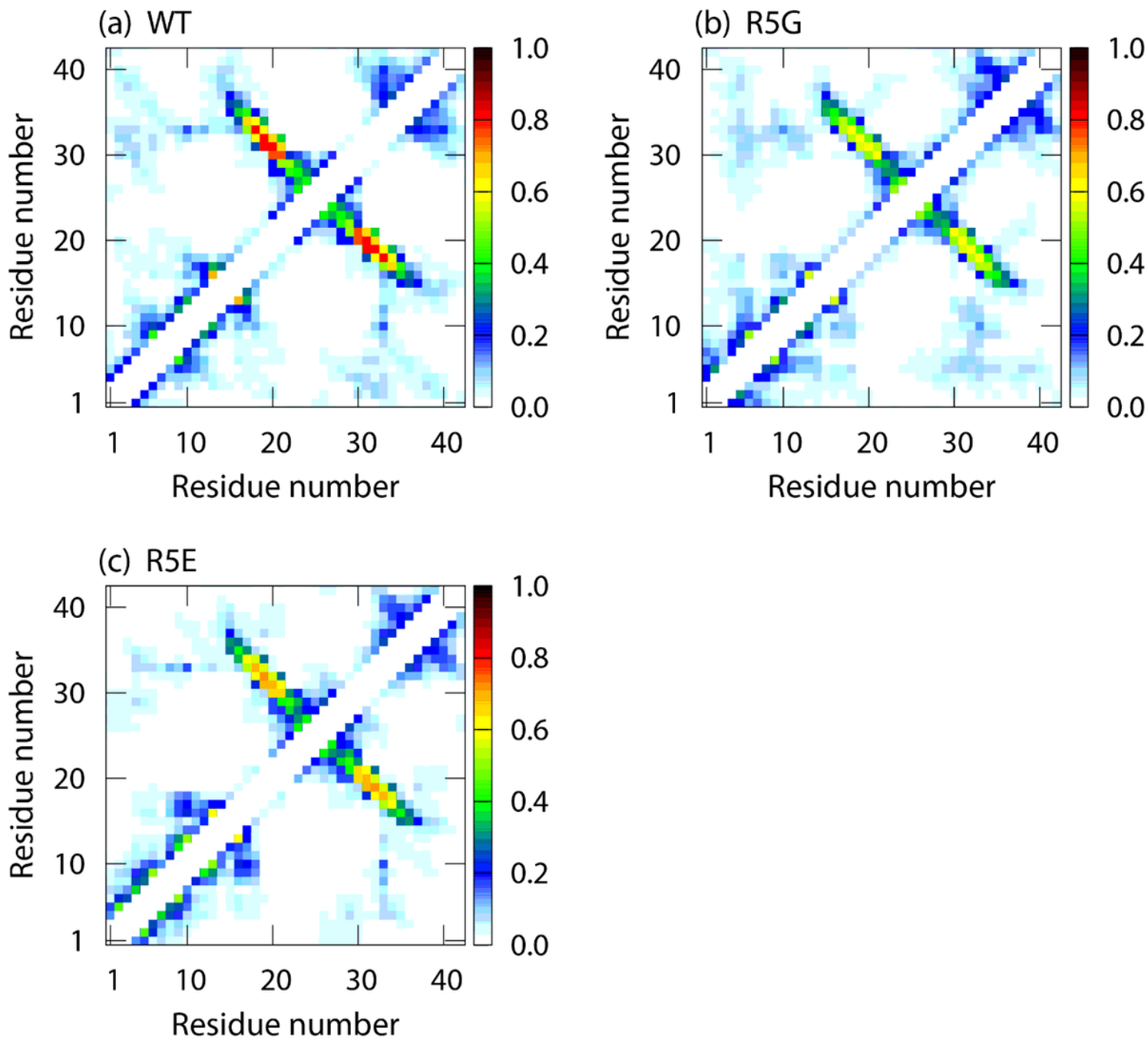


**Figure 9**

Intramolecular contact probabilities of C<sub>α</sub> atoms in the three Ab42 monomers, (a) the wild type, (b) R5G, and (c) R5E.

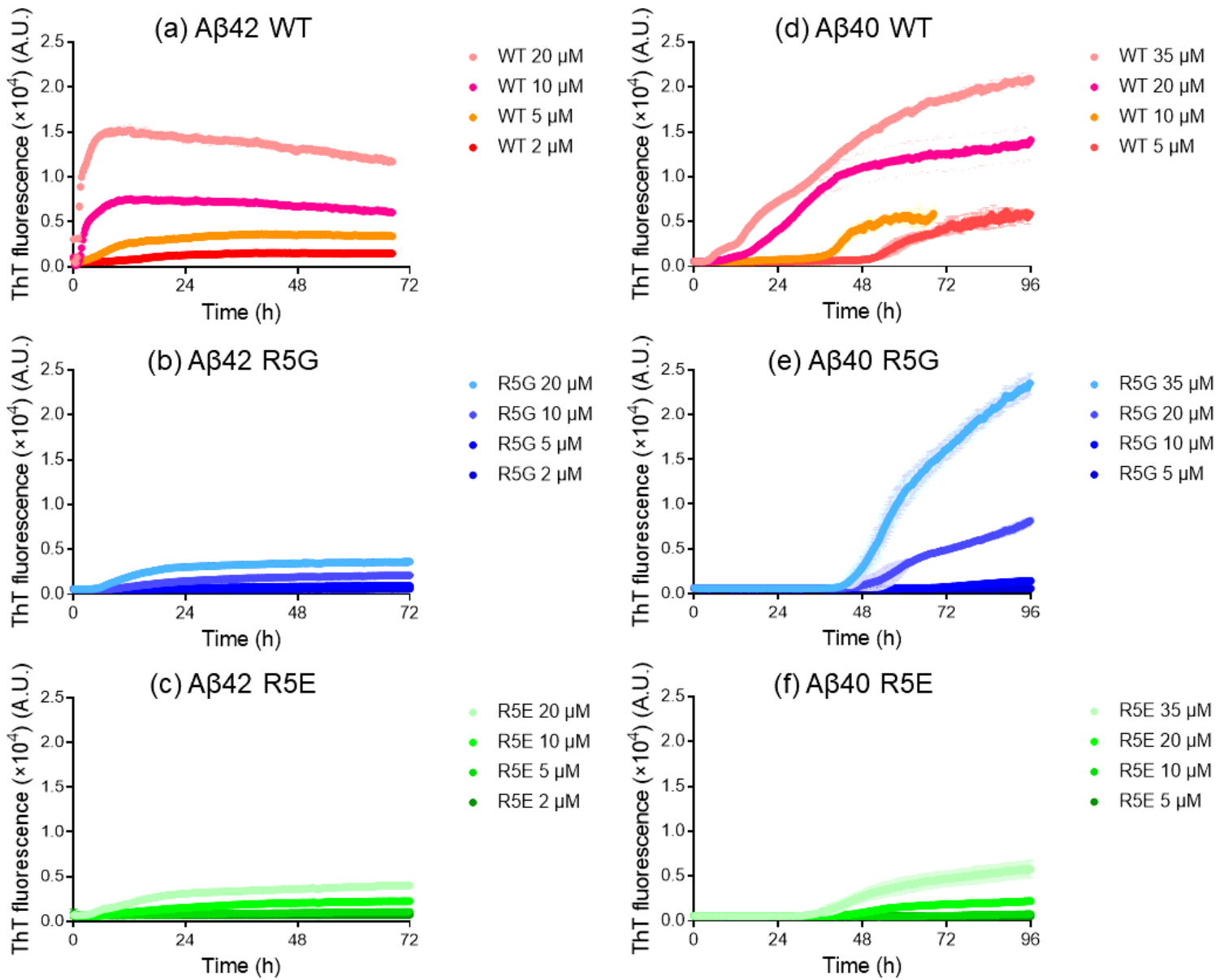


**Figure 10**

Aggregation of (a) the wild type, (b) R5G, and (c) R5E of Ab42s monitored by ThT assay in 20 mM sodium phosphate buffer, pH 7.4. Aggregation of (d) the wild type, (e) R5G, and (f) R5E of Ab40s monitored by ThT assay in 20 mM sodium phosphate buffer, pH 7.4.

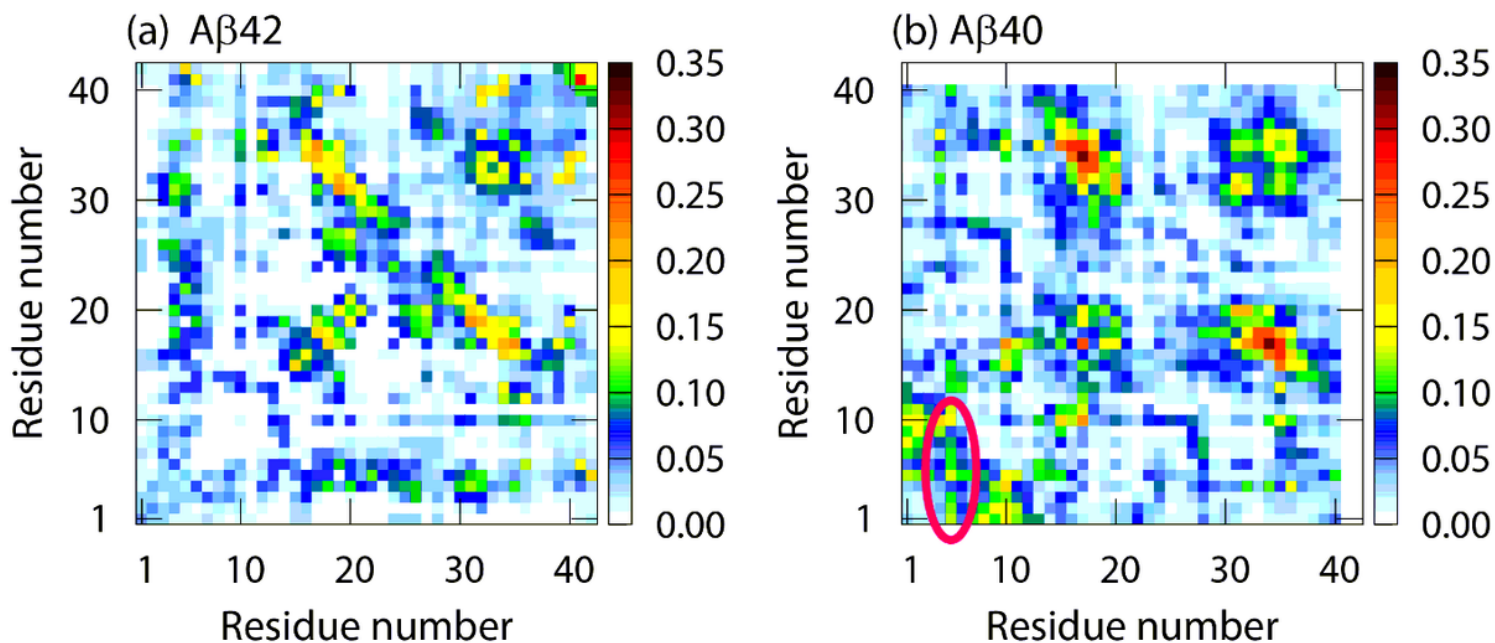


Figure 11

Intermolecular contact probabilities between residues for (a) Ab42 and (b) Ab40. Here, all atoms, including the sidechain atoms, except the hydrogen atoms, are considered in calculating the contact probabilities.

## Supplementary Files

This is a list of supplementary files associated with this preprint. Click to download.

- [abetadimerncsi.pdf](#)
- [movie2.avi](#)
- [movie3.avi](#)